Chapter 1

Graphene, Transition Metal Dichalcogenides, and Perovskite Photodetectors

Zhi Yang, Jinjuan Dou and Minqiang Wang

Additional information is available at the end of the chapter

http://dx.doi.org/10.5772/intechopen.74021

Abstract

Recent years have witnessed a tremendous progress in 2D materials photodetector. Their unique properties including wide photoresponse wavelength, passivated surfaces, strong interaction with incident light, and high mobility enable dramatical superiority in photodetector application. The photophysics, device structure, working mechanism, and performance of three kinds of 2D materials photodetectors including graphene, transition metal dichalcogenides (TMDs), and halide perovskite are discussed in detail to give a profound understanding for the readers. In addition, we highlight the challenges and opportunities faced in studying 2D materials photodetector, and various strategies are summarized to help on the development of photodetection research and find ways to approach major problems.

Keywords: graphene, transition metal dichalcogenides, perovskite, hybrid structure, photodetectors, responsivity, carrier transfer

1. Introduction

Two-dimensional (2D) materials are a class of materials derived from layered van der Waals solids. The in-plane atoms are held together by tight covalent or ionic bonds along 2D directions to form atomic layers, while the atomic layers are bonded together by weak van der Waals interactions along the out-of-plane direction [1–3]. Nicolosi et al. summarized different types of layered materials, which can be grouped into diverse families. The simplest are the atomically thin, hexagonal sheets of graphene and hexagonal boron nitride (h-BN). Other layered materials also include transition metal dichalcogenides (TMDs), black phosphorus (BP), metal halides (such as PbI_2 and $MgBr_2$), layered

metal oxides (such as MnO_2 and MoO_3), layered double hydroxides (LDHs) [such as $Mg_6Al_2(OH)_{16}$], layered III-VIs (such as InSe and GaS), layered V-VIs (such as Bi_2Te_3 and Sb_2Se_3), and halide perovskites [4]. Graphene is composed of a single layer of carbon atoms bonded together in a hexagonal honeycomb lattice, which was firstly obtained by exfoliating graphite using an adhesive tape in 2004 [5]. Then graphene becomes the most famous 2D layered material on the basis of its appealing electronic, optical, mechanical, and thermal properties, and thus Geim and Novosolov were awarded the Nobel Prize in Physics in 2010.

2D materials have many distinctive properties including mechanical stiffness, strength and elasticity and high electrical and thermal conductivity. In this chapter, the optical and electrical properties of 2D materials are cared for photodetector application. Compared with traditional bulk materials, 2D materials have several superiorities as photodetectors. Firstly, 2D materials are sensitive over a wide range of the electromagnetic spectrum including ultraviolet (UV), visible, infrared (IR), and terahertz (THz) (see **Figure 1a**) [6]. The bandgap and photoresponse range of different 2D material photodetectors are summarized in **Figure 1b**. Graphene photodetector can sense over an ultrawide spectrum from UV to IR and even THz due to its zero bandgap and linear dispersion near the Dirac point [7, 8]. TMD photodetectors have a photoresponse over a spectrum from visible to near infrared [9]. The bandgap of BP can be increased from 0.3 eV of bulk to around 2 eV of monolayer, corresponding to near infrared and visible [10]. Halide perovskite photodetectors have a photoresponse over a spectrum from UV to near infrared [11]. Secondly, the surfaces of 2D materials are free of dangling bonds, facilitating the construction of vertical heterojunctions without the restriction of lattice matching and avoiding surface leakage current due to their naturally passivated surfaces, and noise current can be decreased to fairly small order [12]. Thirdly, 2D semiconductors with ultrathin thickness can still strongly interact with incident light resulting from the singularities effect near the conduction and valence band edges [13]. Therefore, 2D semiconductor films are ideal materials for photodetector application.

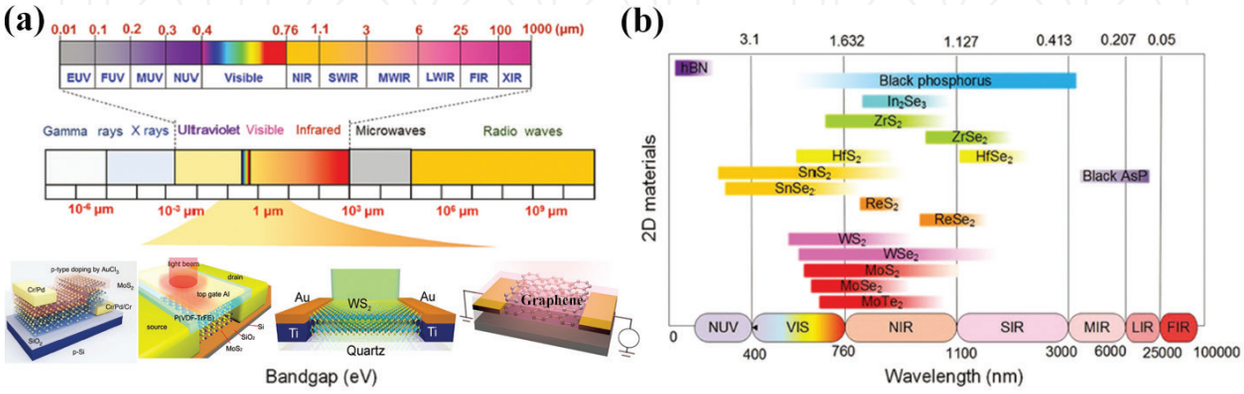

Figure 1. (a) The electromagnetic spectrum of 2D materials photodetector and (b) the gap value and detection range of different 2D materials [6].

2. Graphene photodetector

Graphene is an appealing material for optoelectronic applications. The concentrations of electrons and holes can be as high as 10^{13} cm^{-2}, and their mobilities μ can exceed 15,000 cm^2 V^{-1} s^{-1} even under ambient conditions [14]. Due to its zero bandgap and linear dispersion near the Dirac point, graphene exhibits an extremely broadband absorption from UV to THz. Despite of the atomic layer thickness, graphene absorbs 2.3% of incident photons without significant wavelength dependence [6].

2.1. The physical mechanisms

The physical mechanisms of graphene photodetector including the photoconductive effect, the photovoltaic effect, the photo-thermoelectric effect, the bolometric effect, the photogating effect, and the plasma-wave-assisted mechanism (also called Dyakonov-Shur mechanism) have been reported (**Figure 2**) [15]. Based on the sensing mechanism, photodetectors can be divided into two categories: photon detectors and thermal detectors. Photodetectors that operate via the photovoltaic effect are usually called photodiodes. A photodiode photodetector can function at two modes under illumination: the photovoltaic mode at zero bias and the photoconductive mode under reverse bias [3, 16]. The charge-separation mechanism is shown in **Figure 3**. Photovoltaic effect is based on the separation of photogenerated electron-hole pairs by a built-in electric field at junctions, and electrons and holes are collected at opposite electrodes, which generates a considerable photocurrent (short-circuit current). A photodiode working in photovoltaic mode has the lowest dark current, and an improved detectivity can be obtained. In photoconductive mode, the external electric field with a moderate biasing voltage has the same direction as the built-in one, which increases the separation efficiency of the electron-hole pairs, as well as the response speed due to reduced carrier transit time and lowered diode capacitance. The photo-thermoelectric effect is also called Seebeck effect. Pronounced thermoelectric photocurrent can be generated in graphene by hot carriers, and the temperature differences between carriers are able to produce a significant photoresponse [17]. The bolometric effect is associated with the resistance change produced by heating associated with the incident photons. Instead of generating photocurrent under zero bias, it only modifies the conductance of graphene under high external bias [18–19]. A d.c. voltage is generated

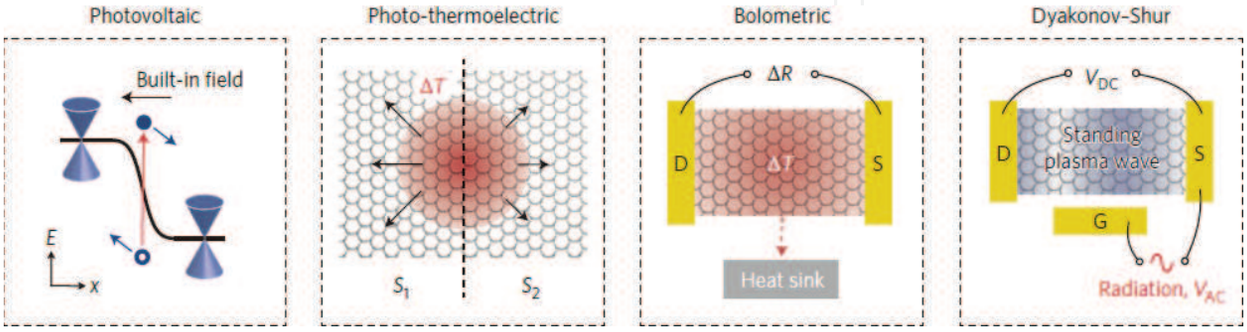

Figure 2. Schematic of the four kinds of graphene photodetection mechanisms [15].

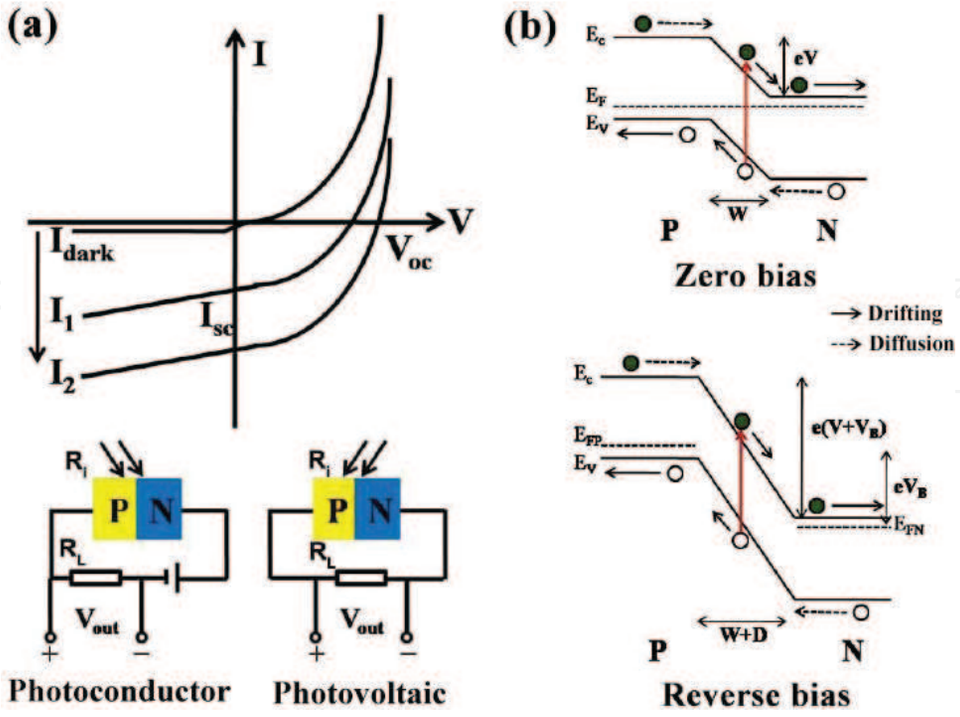

Figure 3. (a) The current-voltage curve of photodiode, and (b) the energy-band diagram of photovoltaic mode and photoconductor mode.

in a field-effect transistor in response to a THz radiation oscillation field through plasma-wave rectification, which was first proposed by Dyakonov and Shur [20]. The graphene photodetector based on plasma-wave-assisted mechanism can be used to integrate with silicon photonics.

2.2. The structure and performance

Here, all graphene photodetectors are based on the photoconductor and photovoltaic effects. The external bias voltage is not desired for graphene photodetectors because a large dark current can be generated as graphene has high conductivity. The built-in electric fields can be introduced by constructing a homogeneous p-n junction, a metal-graphene Schottky junction, or a tunneling barrier junction. Surface chemical modification methods can be adopted for the controllable n- or p-type doping in graphene. Liu et al. fabricated a graphene p-n junction photodiode photodetector through a selected-area chemical doping process, showing its IR detection ability [21]. A metal-graphene-metal (MGM) photodetector can be achieved by taking advantage of the work-function difference between graphene and a contacting metal. In 2009, Xia et al. reported the first graphene photodetector with a 40 GHz bandwidth and a 0.5 mA W^{-1} photoresponsivity (**Figure 4**(**a**, **b**)) [22]. Then they fabricated a MGM photodetector with asymmetric electrodes (Ti and Pd) to extend the operation region, and a photoresponsivity of 6.1 mA W^{-1}, a bandwidth of 16 GHz, and a data rate of 10 Gbit s^{-1} were obtained (**Figure 4** (**c**, **d**)) [23]. In this device, photocurrent is generated by local illumination of one of the metal/graphene interfaces of a back-gated graphene FET. The field arises from charge transfer from the respective contact metal to graphene, and it can be adjusted by choosing proper metal. A graphene double-layer tunneling barrier junction can be used to achieve ultra-broadband and high-sensitivity photodetection. The device is composed of two graphene layers sandwiching a

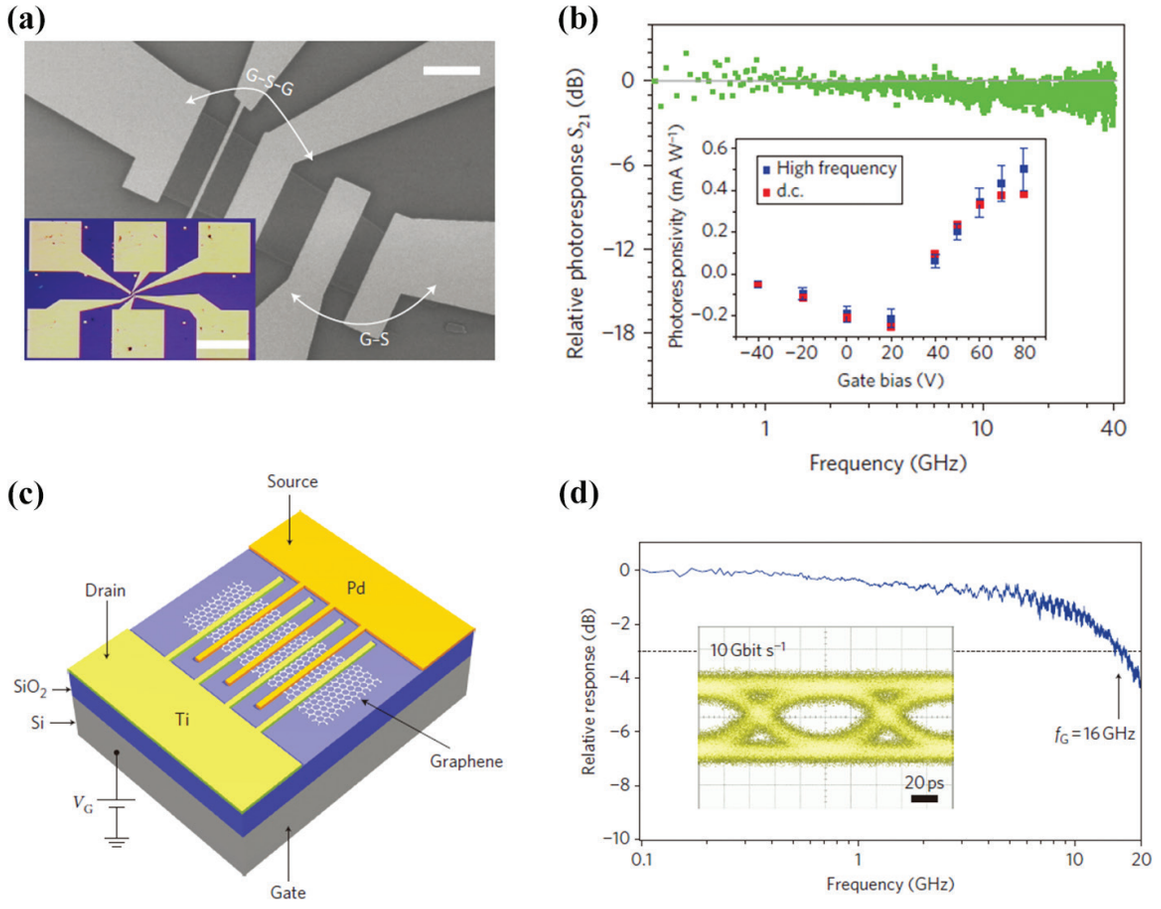

Figure 4. The metal-graphene Schottky junction photodetectors: (a, b) symmetric electrodes and (c, d) asymmetric electrodes [22–23].

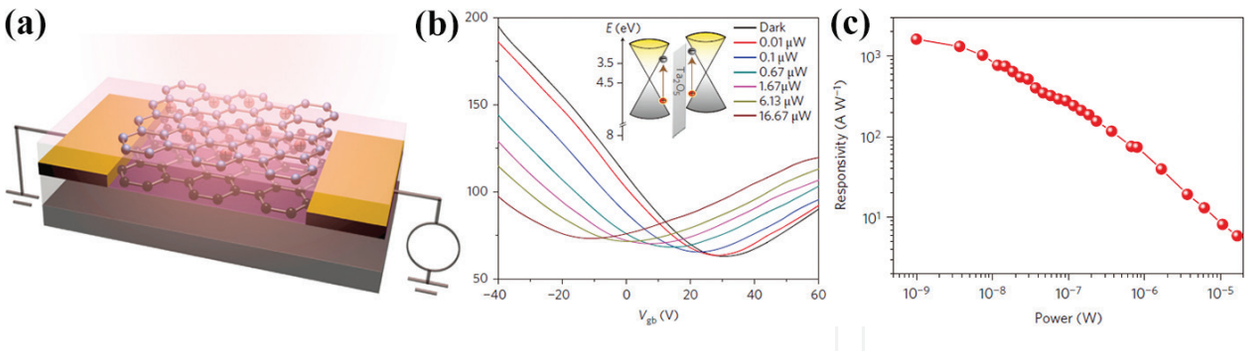

Figure 5. Graphene double-layer tunneling barrier junction photodetectors: (a) schematic of device structure, (b) I-V_g characteristics of the photodetector under different laser powers, and (c) photoresponsivity versus illumination power [24].

5-nm-thick Ta_2O_5 tunnel barrier (**Figure 5**) [24]. The top and bottom graphene layer exhibit shifted Fermi levels about 0.12 eV due to the different extents of interaction with substrates. Under illumination, photogenerated hot carriers in the top graphene tunnel into the bottom layer, leading to a charge build-up on the gate. The devices demonstrated room-temperature photodetection from the visible to the mid-infrared range, with mid-infrared responsivity higher than 1 A/W. Under low excitation power, the device shows a remarkable responsivity of greater than 1000 A/W at 1 V, suggesting the built-in amplification mechanism.

3. TMD photodetector

2D transition metal dichalcogenides (TMDs) include MX_2 (M = Mo, W; X = S, Se, Te) which is formed by covalently bonded X-M-X 2D hexagonal trilayers, and neighboring layers bond with each other via weakly van der Waals forces [25]. Bulk TMDs possess an indirect band gap of 0.9–1.4 eV. Only monolayer TMDs have direct band gap, and the indirect band gap of TMDs is thickness dependent resulting from strong interlayer coupling and quantum confinement effect, contributing to efficient light absorption and emission [26]. The absorption spectrum of TMDs is well matched to the solar spectrum, and the absorption coefficient is typically on the order of 10^4–10^6 cm^{-1} so that more than 95% of the sunlight is absorbed for TMD films with sub-micrometer thickness. The mobility of TMDs increases with the number of layers, typically ranging from 0.2 to 34,000 $cm^2\ V^{-1}\ s^{-1}$ [27]. The charge-carrier density depends on the doping levels and recombination centers, and the typical value is 10^{12} cm^{-2} [28]. Moreover, monolayer TMDs have long-lived excitons because of high binding energies, such as 320 meV for excitons in WS_2 and 20 meV for trions in MoS_2, which are several times higher than those in bulk [29, 30].

3.1. MoS_2 photodetector

Monolayer MoS_2 has a direct bandgap of 1.8 eV, large carrier mobility above 200 $cm^2\ V^{-1}\ s^{-1}$, strong photoluminescence, good chemical stability and mechanical flexibility, and so on [3]. MoS_2-based photodetectors are always in the form of a FET configuration. In 2012, Yin et al. developed a mechanically exfoliated monolayer MoS_2 phototransistor, which has a photoresponsivity of 7.5 mA/W for 750 nm light and a response time of 50 ms [31]. As shown in **Figure 6a**, the cut-off wavelength of photodetector is at ≈670 nm, which agrees well with the bandgap of the monolayer MoS_2. After that, several factors have been investigated to explore how they affect the photoresponse performance. First, the charge trapping in MoS_2 or at the MoS_2/substrate interface plays a key role in the photoresponse process. Lopez-Sanchez et al. obtained a high responsivity up to 880 A/W from a monolayer MoS_2 phototransistor (**Figure 6b**), but the response time can be several seconds, which is influenced by the surroundings of MoS_2 [32]. This is a specific example to demonstrate the effect of trap states on responsivity and response time. Second, the responsivity and response speed are highly dependent on the layer number of MoS_2. Khan et al. reported an increased responsivity and response speed with increasing numbers of MoS_2 layers. They also demonstrated that responsivity is significantly enhanced in N_2 gas environment compared with that in atmospheric environment, indicating that the charge-carrier density can be affected by the oxygen (**Figure 6c, d**) [33]. Third, the preparation methods including mechanically exfoliated, chemical vapor deposition (CVD), liquid exfoliation, and solution synthesis can have a significant effect on photoresponse (**Figure 6e, f**). Similar performance has been reported for mechanically exfoliated and CVD methods, while inferior performance is obtained for solution-processed MoS_2. Besides, electrode contact and surface modification are also reported to affect the performance of MoS_2 photodetector, and several strategies are employed to enhance the photoresponse performance [32, 34, 35]. The photodetector with low Schottky barrier exhibits a very high photo gain, but response speed is slow. On the contrary, a very short response time can be obtained for the photodetector with high Schottky-contact barrier, but the gain decreases by several orders of magnitude [36].

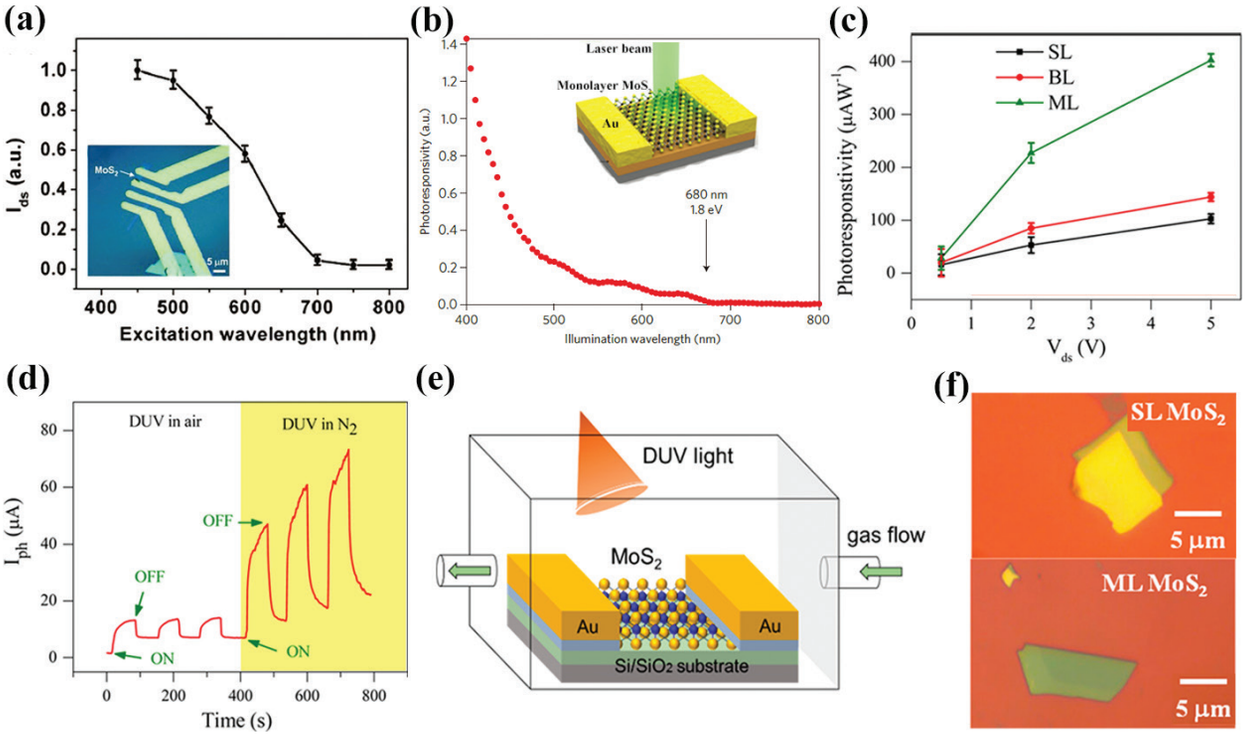

Figure 6. MoS_2 photodetectors based on FET configuration. (a) The dependence of I_{ds} of a single-layer MoS_2 phototransistor on excitation wavelength. Inset shows an optical image of single-layer MoS_2 photodetector device [31] and (b) responsivity of a monolayer MoS_2 phototransistor as a function of incident power. Inset shows the structure and photocurrent spatial map of the MoS_2 photodetector [32]; (c) photoresponsivity of single-layer, bilayer, and multilayer MoS_2 photodetectors as a function of V_{ds}; and (d) time-dependent photoresponse in atmospheric and N_2 environments. (e) Schematic of MoS_2 photodetector prepared by CVD method. (f) Optical images of single layer and multilayer of MoS_2 [33].

3.2. WS_2 photodetector

Monolayer WS_2 has a direct bandgap of 1.98 eV instead of an indirect bandgap of 1.4 eV in the bulk, but its carrier mobility of 0.2 $cm^2 V^{-1} s^{-1}$ is lower than bulk and it also has strong photoluminescence due to high exciton binding energy [26]. WS_2 is also reported to have much smaller effective electron mass, providing better transistor performance than Si as well as MoS_2 [37]. Besides, WS_2 as a potential electronic material is inert, nontoxic, and environmentally friendly. The photoresponse performance of WS_2 photodetector is also affected by the same factors as MoS_2 including the charge trapping induced by substrate and atmosphere environment, the layer number, the preparation methods, electrode contact, and surface modification. Perea-López et al. have studied the photoresponse of CVD-grown few-layer WS_2 photodetector (**Figure 7a**). The responsivity is highly dependent on the excitation wavelength, and the highest photoresponse wavelength is 647 nm. The device shows a maximum photocurrent of 0.6 μA, a responsivity of 92 μA W^{-1}, and a fast response speed of ≈5 ms. The low responsivity is attributed to the high resistances ranging between 10^9 and 10^{12} Ω resulting from the low mobility [38]. Lee et al. reported a mechanically exfoliated WS_2 photodetector with a photoresponsivity of 0.27 A/W and an on/off ratio of 10^2–10^3 [37]. Huo et al. reported that the responsivity of mechanically exfoliated WS_2 photodetector can increase from 5.7 A W^{-1} in vacuum to a maximum of 884 A W^{-1} in an NH_3 atmosphere (**Figure 7b**). The high sensitivity on the surrounding environment can be ascribed to the electron transfer to absorbed gas molecules, demonstrating the role of charge trapping [39]. As shown in **Figure 7c**, Yao et al. prepared

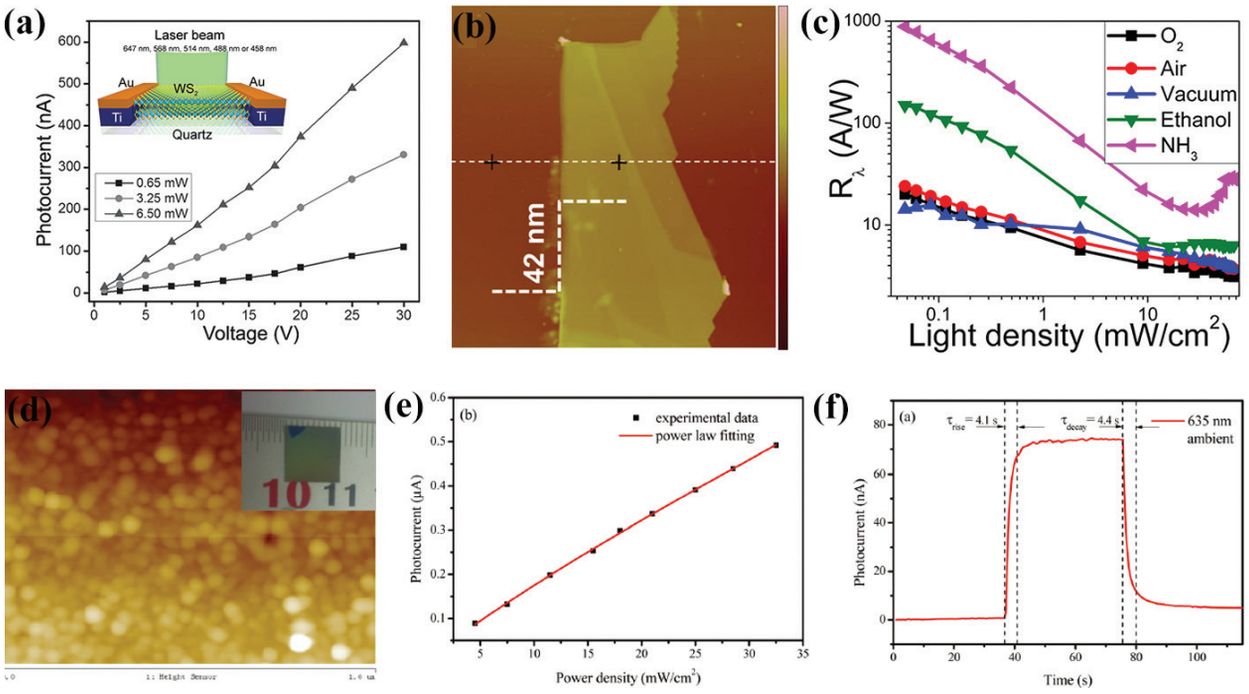

Figure 7. The photoresponse performance of WS_2 photodetectors. (a) IV curve acquired with different laser power irradiation. Inset shows schematic of a few-layered WS_2 photodetector [38], (b) AFM image of the multilayer WS_2 nanoflakes, (c) the relationship between the light intensity and photoresponsivity under various gas atmospheres [39], (d) AFM image and photographs of a large-area multilayered WS_2 film on a 1 × 1 cm^2 Si substrate, (e) power-dependent photocurrent, and (f) temporal photoresponse of the WS_2 photoresistor [40].

multilayer WS_2 films with the size of cm^2 by pulsed-laser deposition method. Benefiting from the large optical absorbance and high carrier mobility (31 cm^2 V^{-1} s^{-1}), the responsivity of the device approaches a high value of 0.51 A W^{-1} in an ambient environment, and it can be further enhanced to 0.7 A W^{-1} in a vacuum environment [40].

4. Perovskite photodetector

Recent years have witnessed the rapid development of the organic-inorganic hybrid halide perovskites. Their exceptional properties including an adjustable spectral absorption range, high carrier mobility, long diffusion lengths, and the affordability of fabrication render them one of the most exceptional optoelectronic materials for photoelectrical device applications especially in photodetectors [41]. Organic-inorganic hybrid halide perovskites have the same chemical formula ABX_3. The A cation can be organic species including $CH_3CH_2NH_3^+$ (EA), $HC(NH_2)_2^+$ (FA), and CH_3NH_3 (MA) or inorganic species such as Cs, Rb, K, and Na, and their ionic radiuses decrease gradually. The A cation is thought no direct contribution toward electronic properties, but its size can alter the degree of distortion that in turn affects electronic properties [42]. The B metal cation can be group IV metal such as Pb^{2+}, Sn^{2+}, and Ge^{2+} in a divalent oxidation state, and the Pb^{2+} has superior stability than Sn^{2+} and Ge^{2+}. The halide anion can be the most effectively varied component. In general, with increasing ionic radius, a narrower bandgap can be obtained, resulting in that absorption spectra shift to longer wavelengths.

Perovskites have a large absorption coefficient, so strong optical absorbance across the entire visible spectrum can be achieved for a thin thickness less than 500 nm, facilitating the collection of charge carriers [43]. Moreover, $MAPbI_3$ has been reported with the carrier diffusion lengths up to 100 nm for both electrons and holes, and exceeding 1 μm has been reported in the $MAPbI_{3-x}Cl_x$, resulting from long carrier lifetime and large carrier mobility [44, 45]. So far, perovskite photodetectors have been widely reported from different aspects including composition engineering such as the organic-inorganic hybrid $MAPbX_3$ (X = Cl, Br, I) and all-inorganic $CsPbX_3$ (X = Cl, Br, I) perovskites, morphology such as compact polycrystalline films and nanocrystal films (quantum dots, nanocubes, nanowires, nanoplatelets, and nanosheets), device structure such as photoconductor and photodiode, and so on. Compared with organic-inorganic perovskite, all-inorganic perovskite exhibits better air stability.

4.1. 2D perovskite photodetector

2D halide perovskites with different morphologies including microdisks, nanoplatelets, and nanosheets (NSs) have been synthesized via both CVD and colloidal chemistry methods. Many features including high photoluminescence (PL) quantum yield, quantum confinement effect, increased exciton binding energy, and long electron diffusion length have been demonstrated. In 2015, Jang et al. synthesized $MAPbBr_3$ nanoplatelets with the length of 70 nm and the thickness of 15 nm by colloidal chemistry method, and mixed halide perovskite ($MAPbBr_{3-x}Cl_x$ and $MAPbBr_{3-x}I_x$) nanoplatelets were obtained by anion-exchange reaction in solution. The full-range band gap tuning over a wide range (1.6–3 eV) was demonstrated in **Figure 8a** [46]. By comparing photoresponse performance in **Figure 8b** and **c**, $MAPbBrI_2$ has a larger photocurrent than $MAPbBr_3$ under the same irradiation condition, which may result from its stronger light absorption. Next, Liu et al. synthesized triangle 2D $MAPbI_3$ NSs with thinner thickness of several nanometers and larger lateral sizes of several micrometers based on two-step CVD method. A photoconductor photodetector was fabricated in the form of a FET configuration (**Figure 8d** and **e**). High responsivities of 22 12 A W^{-1} at 1 V bias voltage were obtained under irradiations of 405 nm laser with 0.07 mW cm^{-2}. The response or recovery time was shorter than 20 or 40 ms upon 405 nm irradiation (**Figure 8f** and **g**) [47]. The excellent photoresponse properties make this 2D perovskite promise for photodetection applications.

2D all-inorganic perovskites are also reported to fabricate high-performance photodetectors. In particular, $CsPbBr_3$ NSs has been widely studied on synthesis, photophysics, electrical property, and device application due to its high air stability. 2D $CsPbBr_3$ perovskite is formed by incorporating Cs^+ cations into a 2D sheet of $PbBr_4^{2-}$ octahedra of which six Br atoms surround each Pb atom and four in-plane Br atoms are being shared by two octahedrons [11]. Bulk $CsPbBr_3$ has been reported to possess a thermodynamically orthorhombic structure at room temperature, and it can transform to tetragonal and cubic phases at 88 and 130°C, respectively [48]. However, the cubic phase could be preserved at room temperature owing to a large number of surfaces. Both cubic and orthorhombic phases are reported for $CsPbBr_3$ NSs by different groups [49, 50]. In terms of well-controlled synthesis, Akkerman et al. synthesized few-layer $CsPbBr_3$ NSs with monolayer-level thickness control [51]. Shamsi et al. synthesized few-layer $CsPbBr_3$ NSs with lateral dimensions up to a micrometer size. [52] For photophysics, Li et al. measured PL decay time of 2 ns and exciton binding energy of 120 meV for $CsPbBr_3$

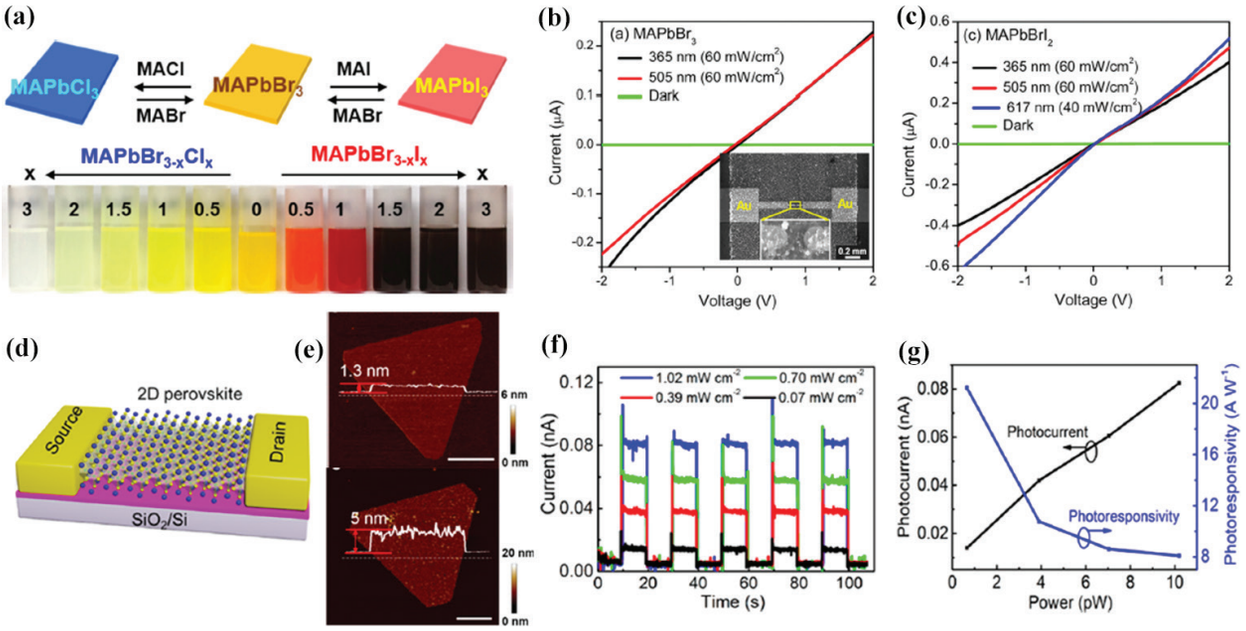

Figure 8. (a) Schematic for $MAPbX_3$ NSs synthesized by anion-exchange reaction. I–V characteristics of (b) $MAPbBr_3$ and (c) $MAPbBrI_2$ NSs film under different irradiation and dark conditions, (d) schematic of the 2D $MAPbI_3$ NSs photodetector [46], (e) AFM images of $MAPbI_3$ NSs with different thicknesses, (f) time-dependent photocurrent measurement, and (g) photocurrent and photoresponsivity versus optical illumination power under the 405 nm irradiation [47].

nanoplates with a thickness of 3.4 nm and the lateral dimensions of 20.2 nm [53]. Our group reported a larger exciton binding energy of 231.6 meV for $CsPbBr_3$ NSs with larger lateral dimensions of 700 nm and a thickness of 1.8 nm based on the absorption spectrum fitting with a quantum-well absorption model (**Figure 9a–c**). At the same time, high carrier mobility of 77.9 $cm^2 V^{-1} s^{-1}$ was obtained by the Hall effect and transient photoconductivity measurements [54]. There are some reports on 2D $CsPbBr_3$ NSs photodetector application. In 2016, Song et al. fabricated flexible $CsPbBr_3$ NS film visible-light photodetectors with a light on/off ratio of $>10^3$, a R of 0.64 A W^{-1}, and an EQE of 54% under 442 nm light at a power of 0.35 mW cm^{-2}. The response and recovery time were measured to be 0.019 or 0.025 ms, respectively. A high stability and outstanding flexibility (>10,000 cycles) were also obtained [55]. This work demonstrates that all-inorganic perovskite $CsPbBr_3$ NSs have a great potential in photodetector application. Next, Lv et al. reported a similar result on $CsPbBr_3$ NSs photodetectors [56]. Then, our group reported that the responsivity could be improved by the annealing, which was demonstrated to increase coupling energy but decrease exciton binding energy resulting from ligand rearrangement. Tunneling instead of resonant energy transfer as a dominant way of exciton dissociation contributed to a high charge transfer rate. This exciton dissociation mechanism was proposed based on microscopic KPFM results (**Figure 9d**). As shown in **Figure 9e** and **f**, the response and recovery time were short, and the largest responsivity of 0.53 A W^{-1} could be obtained under the 525 nm irradiation with the intensity of 0.009 mW cm^{-2} [54].

4.2. Perovskite/graphene hybrid photodetector

Despite that the perovskites with different compositions, morphologies, and structures have been reported as photodetectors with high performance, their responsivity can be further

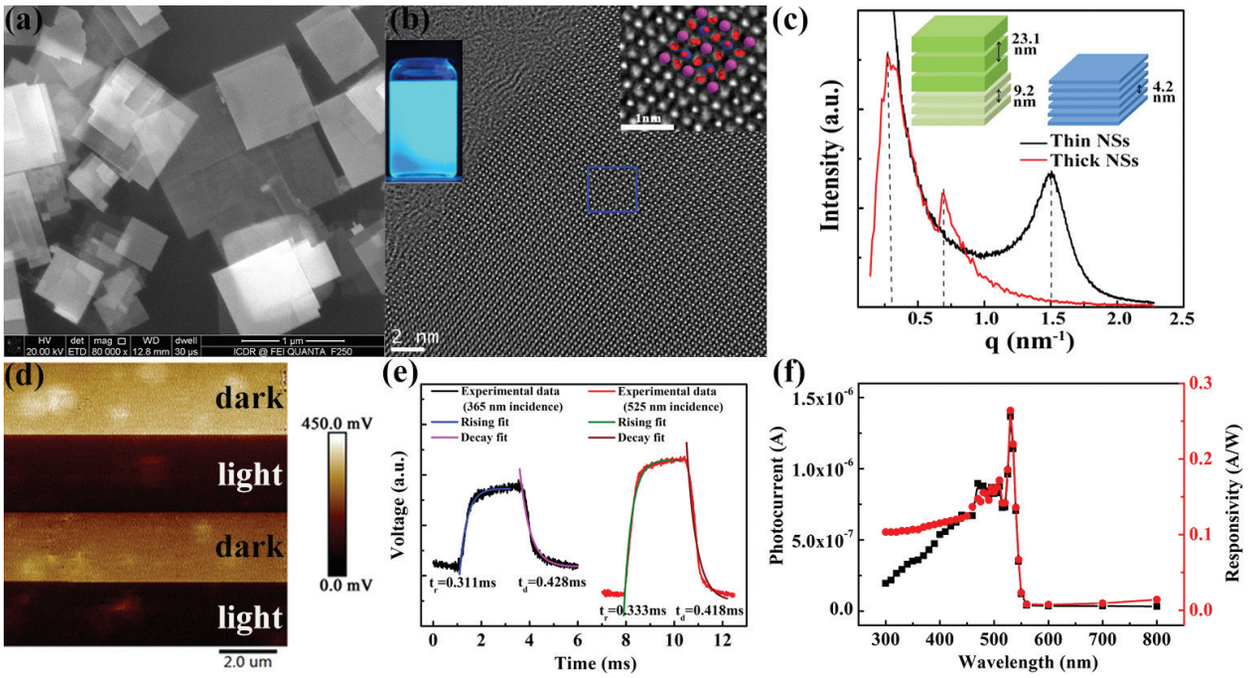

Figure 9. (a) Scanning electron microscope (SEM) image, (b) transmission electron microscopy (TEM) image, and (c) small-angle X-ray scattering (SAXS) patterns of $CsPbBr_3$ NSs, (d) Kelvin probe force microscopy (KPFM) surface potential mapping, (e) transient photoresponse curves, and (f) the wavelength-dependent photocurrent and responsivity curves of $CsPbBr_3$ NS film photodetector [54].

improved by constructing hybrid structure. A promising strategy is based on hybrid phototransistors, where light is efficiently absorbed by perovskite layer while photogenerated carriers can transfer into conducting layer such as graphene, and high gain can be obtained from one carrier that recirculate many times within the lifetimes of the opposite charges [3]. For this hybrid photodetector, graphene is firstly transferred on the FET configuration substrate, and then perovskites including polycrystalline film or nanocrystal can be deposited on the graphene. In 2015, Lee et al. fabricated the $MAPbI_3$/graphene hybrid photodetector, and a dramatic PL quenching was observed for hybrid film resulting from effective charge-carrier transfer through π-π interaction between perovskite and sp^2 hybridized graphene (**Figure 10a, b**). The device exhibited a broad spectral photoresponsivity across the visible range. The photoresponsivity and effective quantum efficiency (EQE) were 180 A/W and 5×10^4% at a relatively high illumination power of 1 μW, respectively (**Figure 10c**). The device also exhibited good on-off switching, and response and recovery times were 87 and 540 ms (**Figure 10d**) [57]. The success of this novel perovskite/graphene hybrid photodetector is a powerful evidence to demonstrate efficient hybrid structure. Instead of compact polycrystalline perovskite film, Wang et al. reported a high-performance perovskite/graphene hybrid photodetector consisting of graphene covered with a layer of dispersive $MAPbBr_2I$ islands. A photoconductive gain of 10^9, a responsivity of 6.0×10^5 A W^{-1}, and a broadband detection across UV-visible are obtained. The photoresponse mechanism was discussed deeply. Under illumination, electron-hole pairs were generated in perovskite and then separated at the heterojunction interface. The holes were transferred to graphene sheets, and electrons were trapped in perovskite with a quite long lifetime, inducing a photogating effect [58]. Then, Qian et al. fabricated a nitrogen-doped graphene quantum dots (NGQDs)-$MAPbI_3$/reduced graphene oxide (rGO) transistor, exhibiting a high responsivity of 1.92×10^4 A/W and

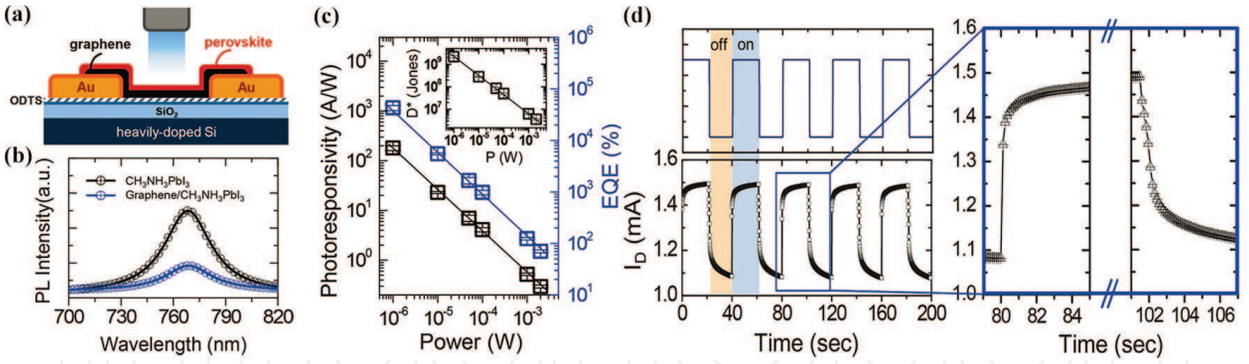

Figure 10. Graphene/$MAPbI_3$ hybrid photodetector. (a) Schematic diagram of the device, (b) PL spectra of the pristine $MAPbI_3$ and graphene/$MAPbI_3$ hybrid films upon excitation at 532 nm, and (c) responsivity and EQE vs. illumination power at 520 nm wavelength. The inset shows the photodetectivity vs. illumination power, (d) Photo-switching characteristics of the photodetector under alternating dark and light illumination (500 μW, 520 nm). The gate and drain voltages were 0 and 0.1 V, respectively [57].

a short response and recovery time of 10 ms. The outstanding performance was attributed to that NGQDs offer an effective path for electron transfer from perovskite to the rGO [59]. Despite high responsivity, perovskite/graphene hybrid photodetectors suffer from a large dark current about mA order because of ultrahigh conductivity of bottom graphene layer, resulting in high noise level.

Besides the lateral photoconductor structure, a vertical graphene/perovskite/graphene (GPG) photodetector has also been fabricated, and higher responsivity is achieved due to its shorter carrier extraction length. Duan's group fabricated a series of single 2D material heterojunction. Wang et al. reported a graphene/$CsPbBr_3$ microplate/graphene sandwiched vertical photodetector by growing $CsPbBr_3$ microplates on an exfoliated graphene flake, followed by the dry transfer of a second layer of graphene (**Figure 11a**). As shown in **Figure 11b**, the photocurrent rapidly increased with the light power, and the photocurrent versus bias curves were nonlinear, indicating the presence of a contact barrier. The responsivity decreases with the increasing light power density, and the maximum responsivity exceeds 10^5 A/W (**Figure 11c**) [60]. Besides, Cheng et al. fabricated a graphene/$MAPbI_3$/graphene photodetector, delivering a high responsivity of 950 A W^{-1} and a high photoconductive gain of 2200 at 1 V bias under a 1.52 nW irradiation of 532 nm laser (**Figure 11d** and **e**). It also exhibited good and reproducible photo-switching behavior with response and recovery time of 22 and 37 ms. The photocurrent mapping showed uniformly contribution from the overlapping area, indicating that the majority of photoinduced carriers travel in vertical direction (**Figure 11f**) [61].

4.3. Perovskite/TMDs hybrid photodetector

Compared with perovskite/graphene hybrid photodetector, perovskite/TMD hybrid photodetector has a significant lower dark current. TMD layer serves as both light absorbers and carrier transport layer, while perovskite as sensitized layer can enhance light absorbance and extend the detection range. The heterojunction formed between perovskite and TMD layer

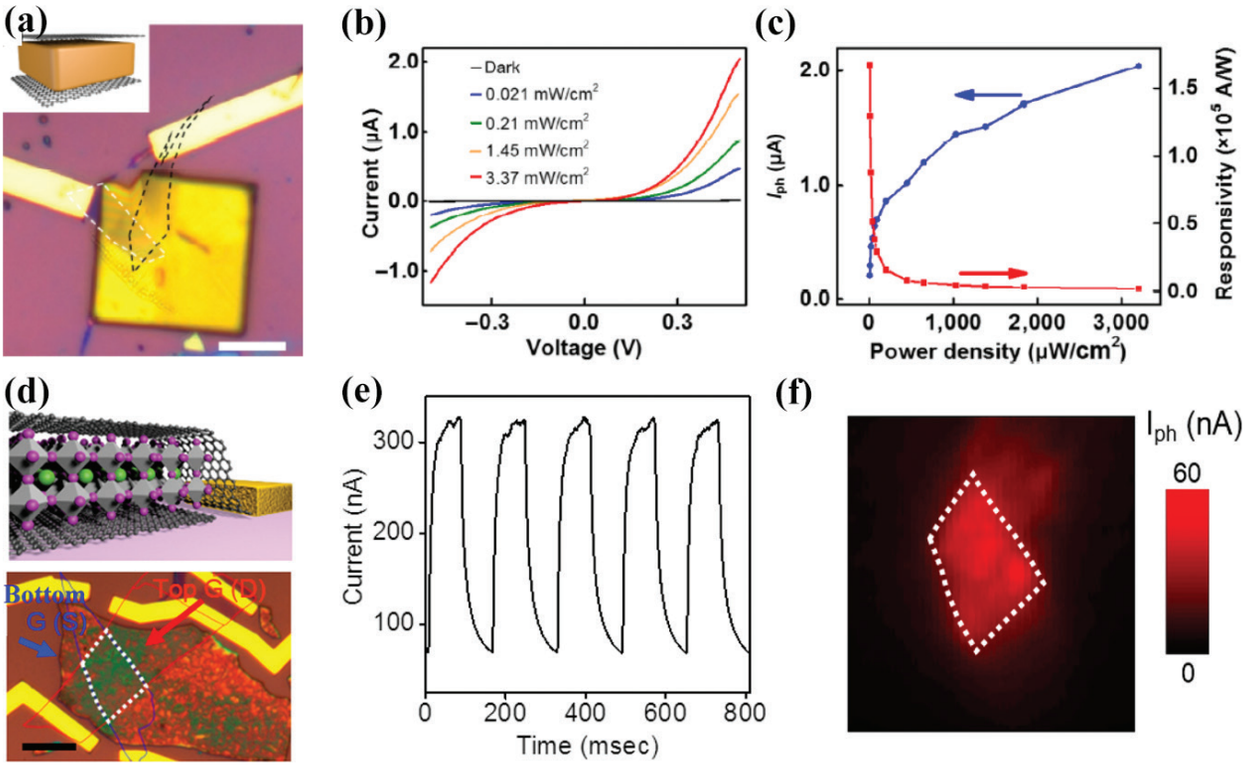

Figure 11. Graphene/$CsPbBr_3$ microplate/graphene photodetector. (a) Optical microscope image of a vertical heterostructure. The inset shows a device schematic, (b) photocurrent versus bias in the dark and under different illumination light power densities, (c) power density dependence of the photocurrent and responsivity [60], graphene/$MAPbI_3$ nanoflakes/graphene photodetector, (d) device schematic, (e) photo-switching characteristics of the photodetector under alternating dark and light illumination, and (f) the corresponding photocurrent mapping [61].

can promote the carrier transfer, contributing to a high responsivity and fast response speed. In 2016, Ma et al. fabricated a hybrid perovskite $MAPbI_3$ and TMDs material WS_2 planar photoconductor detector for the first time. Both $MAPbI_3$ and WS_2 layers contacted with Au electrodes, which could transport photocarriers as parallel channels (**Figure 12a**). From the band structures of hybrid bilayer in **Figure 12b**, photogenerated charges were separated at the interface due to the Fermi level difference, which reduced the charge recombination and enhanced the carrier separation. The significant PL quenching for both $MAPbI_3$ and WS_2 was observed, indicating efficient charge transfer at the interface and exciton dissociation (**Figure 12d**). Furthermore, they proposed the photoresponse mechanism. In dark, the charge transfer at the interface lowers (raises) the Fermi level of WS_2 (perovskite), leading to the formation of depletion regions, suppressing the dark current. Under the light illumination, excitons are generated in the perovskite film, and electrons are transferred to WS_2 film, which raises (lowers) the Fermi level of WS_2 (perovskite) and reduces the Schottky barriers at contacts, resulting in the high photocurrent (**Figure 12c**). The device exhibited a high on/off ratios of $\approx 10^5$ and a high responsivity of ≈ 17 A W^{-1}. Owing to the high mobility of the WS_2 monolayer and the efficient interfacial charge separation, the response speed of the hybrid photodetector was enhanced by four orders of magnitude compared to the reference perovskite single layer (**Figure 12e** and **f**) [62].

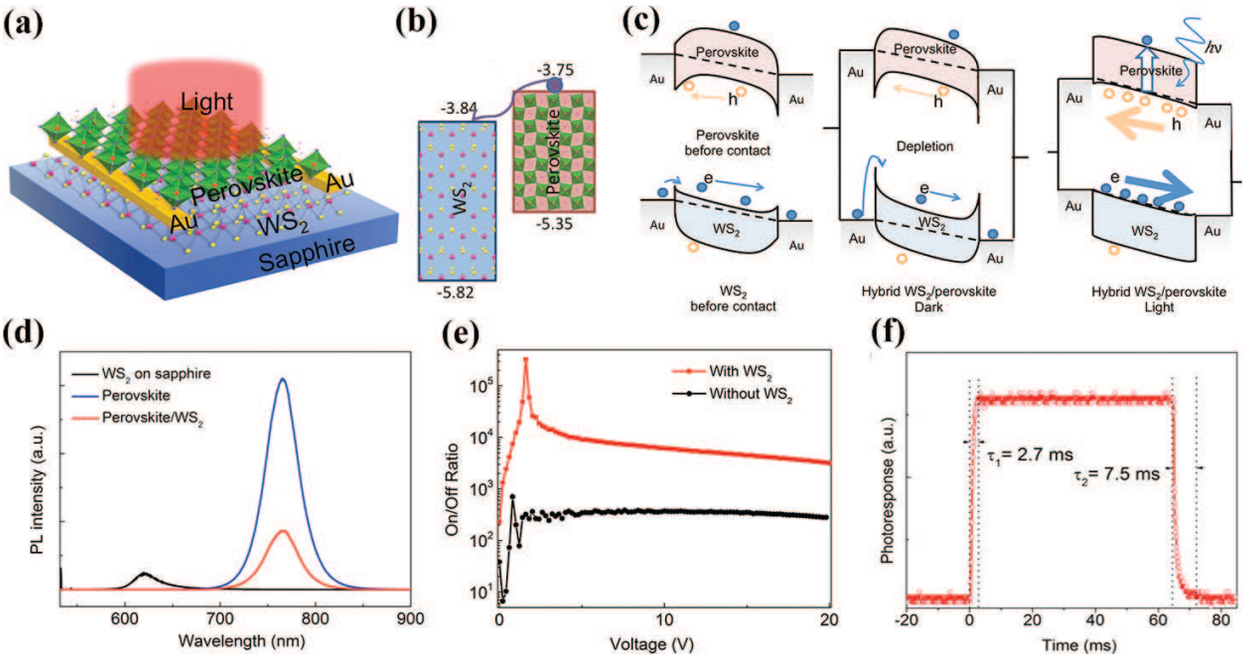

Figure 12. WS_2/$MAPbI_3$ hybrid photodetector. (a) Schematic device structure; (b) band structures of hybrid bilayer; (c) working mechanism of hybrid photodetector; (d) PL spectra of WS_2, perovskite, and hybrid bilayer upon excitation at 532 nm; (e) bias dependence of the on/off ratios; and (f) time-dependent photoresponse [62].

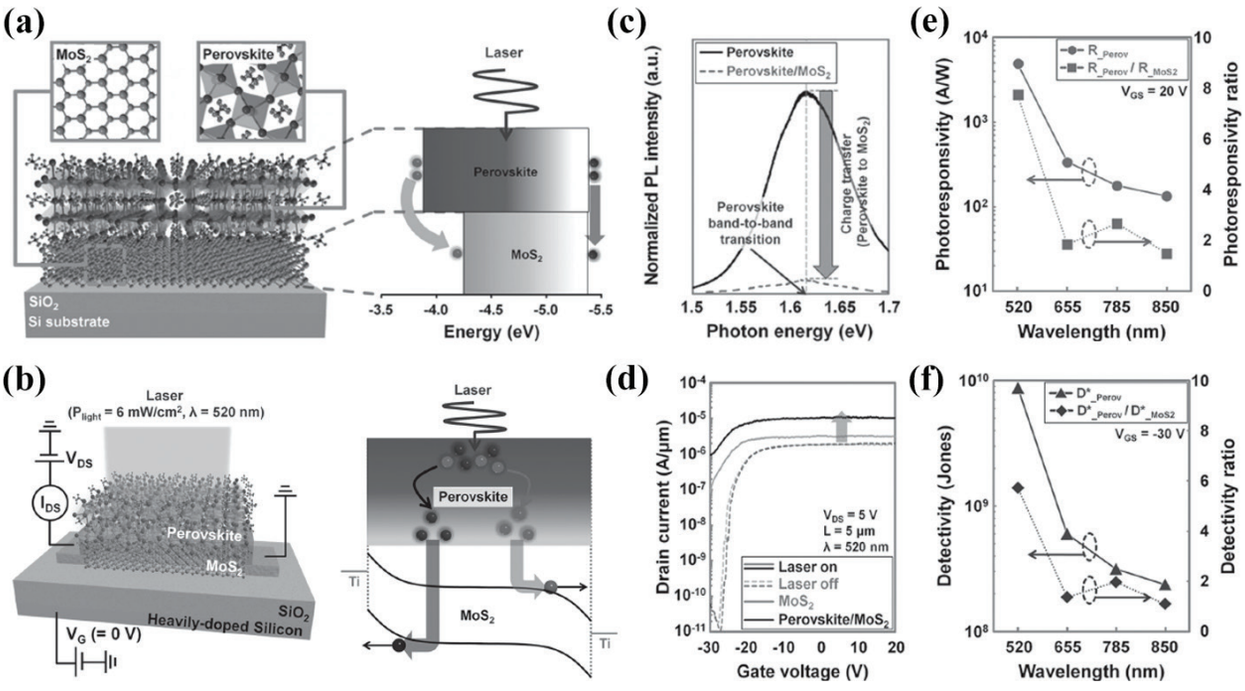

Figure 13. MoS_2/$MAPbI_3$ hybrid photodetector. (a) Schematic device structure and energy-band diagram, (b) schematic device structure and energy-band diagram of photodetector under 5 V bias voltage and laser exposure, (c) PL spectra of perovskite and perovskite/MoS_2 hybrid bilayer, (d) IV characteristics of MoS_2 and perovskite/MoS_2 photodetectors under both dark and illuminated conditions, (e) photoresponsivity as a function of the incidence wavelength, and (f) photo-switching characteristics [63].

At the same time, Kang et al. developed an ultrahigh-performance $MoS_2/MAPbI_3$ hybrid photodetector by using mechanically exfoliated 25-nm-thick MoS_2 nanoflakes [63]. Similar with the $WS_2/MAPbI_3$ hybrid bilayer, the photogenerated electrons in perovskite are thought to reach the MoS_2 layer through diffusion (**Figure 13a**). The significant PL quenching for hybrid bilayer was also observed, indicating the charge transfer at the interface (**Figure 13c**). Under the bias voltage and laser illumination, electron-hole pairs generated in perovskite were separated based on the ambipolar charge transport property of the perovskite and diffuse into the MoS_2 region, followed by the carrier collection step caused by the electric field in the Ti-MoS_2 junctions (**Figure 13b**). The photocurrent of hybrid photodetector has increased by one order than MoS_2 photodetector when V_G was −30 V(**Figure 13d**). The photoresponsivity of the hybrid photodetector and their ratios as a function of wavelength is shown in **Figure 13e**. In the case of the 520 nm laser, the photoresponsivity was highly enhanced by factors of 7.7 (from 636 to 4.9×10^3 A W^{-1}). The response and recovery time were also decreased for hybrid photodetector, but they are quite long compared with $WS_2/MAPbI_3$ hybrid photodetector (**Figure 13f**). Then, Lu et al. reported a $WSe_2/MAPbI_3$ hybrid photodetector with a photoresponsivity of 110 A W^{-1}, a high EQE of 2.5×10^4%, and a high D* of 2.2×10^{11} Jones [64]. In all, the outstanding photoresponse performance of perovskite/TMDs hybrid photodetector demonstrates this strategy as an efficient route to improve the performance of 2D material photodetector.

5. Summary and outlook

The distinctive optical and electrical properties enable 2D materials as an ideal and powerful candidate in photodetector application. The superiorities of 2D materials include a wide range of photoresponse wavelength (graphene is from UV to THz, TMDs is from visible to near infrared, halide perovskite is from UV to near infrared), facilitating the construction of vertical heterojunctions due to their naturally passivated surfaces, and the strong interaction with incident light resulting from the singularities effect near the conduction and valence band edges. This chapter has introduced the photophysics, device structure, working mechanism, and performance of three kinds of 2D materials photodetectors including graphene, TMDs, and halide perovskite. For graphene photodetector, four kinds of physical mechanisms are discussed, and the graphene p-n junction and metal-graphene Schottky junction are based on photovoltaic and photoconductor effects, respectively. These two effects also work for most of the 2D materials photodetectors. Generally, graphene photodetector has a wide sensitive wavelength and fast response speed, but it also suffers from a low responsivity and a high dark current. For TMD photodetector, there are the same performance influence factors, such as the charge trapping induced by substrate and atmosphere environment, the layer number, the preparation methods, electrode contact, and surface modification. However, the photoresponse performance is also determined by the photophysical parameters including mobility and absorption coefficient. For example, MoS_2 photodetector has a higher responsivity than WS_2 because of its high mobility. For 2D halide photodetector, the high absorption and mobility promote the high photoresponse performance of $MAPbBr_3$ nanoplatelets and $CsPbBr_3$ nanosheets. Furthermore, both the perovskite/graphene and perovskite/TMD hybrid

structures are employed to enhance the photoresponse based on reduced the charge recombination and enhanced the carrier separation due to band difference. In summary, the 2D materials show their unique superiority in photodetector application.

In spite of the great success for 2D materials photodetectors, it is admitted that lots of challenges still remain. The dark current of graphene photodetector is too large, resulting in a high noise. The sensitive to environment such as oxygen and water is an unfavorable factor to TMDs and perovskite photodetectors, which is the origin of the device instability. To solve these problems, the novel 2D materials, approaches, and hybrid structure should be developed to meet the requirement for practical applications. First, the responsivity and response speed can be enhanced by exploring novel 2D materials with controllable preparation method. Second, novel approaches for chemical doping and surface treatment should be investigated, which has been proved as a feasible strategy for improving or manipulating device performance. Third, new hybrid photodetectors should be focused to demonstrate the increased responsivity resulting from efficient carriers transfer. Both materials engineering and device structure design are important to achieve high and reliable photoresponse performance for pursuing practical application of 2D materials photodetectors in the future.

Acknowledgements

This work was supported by Natural Science Foundation of China (NSFC grant nos. 61604122, 51572216, and 61774124) and China Postdoctoral Science Foundation (grant 2017M613139).

Author details

Zhi Yang*, Jinjuan Dou and Minqiang Wang

*Address all correspondence to: yangzhi029@xjtu.edu.cn

Electronic Materials Research Laboratory (EMRL), Key Laboratory of Education Ministry, International Center for Dielectric Research, Shaanxi Engineering Research Center of Advanced Energy Materials and Devices, Xi'an Jiaotong University, Xi'an, China

References

[1] Novoselov KS, Jiang D, Schedin F, Booth TJ, Khotkevich VV, Morozov SV, Geim AK. Two-dimensional atomic crystals. In: Proceedings of the National Academy of Sciences. 2005;**102**:10451

[2] Xu M, Liang T, Shi M, Chen H. Graphene-like two-dimensional materials. Chemical Reviews. 2013;**113**:3766

[3] Xie C, Mak C, Tao X, Yan F. Photodetectors based on two-Dimensional layered materials beyond graphene. Advanced Functional Materials. 2017;**27**:1603886

[4] Nicolosi V, Chhowalla M, Kanatzidis MG, Strano MS, Coleman JN. Liquid exfoliation of layered materials. Science. 2013;**340**:1226419

[5] Novoselov KS, Geim AK, Morozov SV, Jiang D, Zhang Y, Dubonos SV, Grigorieva1 IV, Firso AA. Electric field effect in atomically thin carbon films. Science. 2004;**306**:666

[6] Wang J, Fang H, Wang X, Chen X, Liu W, Hu W. Recent progress on localized field enhanced two-dimensional material photodetectors from ultraviolet—visible to infrared. Small. 2017;**13**:1700894

[7] Meric I, Han MY, Young AF, Ozyilmaz B, Kim P, Shepard KL. Current saturation in zero-bandgap, top-gated graphene field-effect transistors. Nature Nanotechnology. 2008;**3**:654

[8] Bonaccorso F, Sun Z, Hasan T, Ferrari AC. Graphene photonics and optoelectronics. Nature Photonics. 2010;**4**:611

[9] Chhowalla M, Shin HS, Eda G, Li LJ, Loh KP, Zhang H. The chemistry of two-dimensional layered transition metal. Nature Chemistry. 2013;**5**:263

[10] Tran V, Soklaski R, Liang Y, Yang L. Layer-controlled band gap and anisotropic excitons in few-layer black phosphorus. Physical Review B. 2014;**89**:235319

[11] Chen S, Shi G. Two-dimensional materials for halide perovskite-based optoelectronic devices. Advanced Materials. 2017;**29**:1605448

[12] Geim AK, Grigorieva IV. Van der Waals heterostructures. Nature. 2013;**499**:419

[13] Britnell L, Ribeiro RM, Eckmann A, Jalil R, Belle BD, Mishchenko A, et al. Strong light-matter interactions in heterostructures of atomically thin films. Science. 2013;**340**:1311

[14] Geim AK, Novoselov KS. The rise of graphene. Nature Materials. 2007;**6**:183

[15] Koppens FHL, Mueller T, Avouris P, Ferrari AC, Vitiello MS, Polini M. Photodetectors based on graphene, other two-dimensional materials and hybrid systems. Nature Nanotechnology. 2014;**9**:780

[16] Konstantatos G, Sargent EH. Nanostructured materials for photon detection. Nature Nanotechnology. 2010;**5**:391

[17] Bistritzer R, MacDonald AH. Electronic cooling in graphene. Physical Review Letters. 2009;**102**:206410

[18] Yan J, Kim MH, Elle JA, Sushkov AB, Jenkins GS, Milchberg HM, et al. Dual-gated bilayer graphene hot-electron bolometer. Nature Nanotechnology. 2012;**7**:472

[19] Wang X, Gan G. The nonlinear electronic transport in multilayer graphene on silicon-on-insulator substrates. Chinese Physics B. 2017;**26**:034203

[20] Dyakonov M, Shur M. Shallow water analogy for a ballistic field effect transistor: New mechanism of plasma wave generation by dc current. Physical Review Letters. 1993;**71**:2465

[21] Liu N, Tian H, Schwartz G, JBH Tok TR, Bao Z. Large-area, transparent, and flexible infrared photodetector fabricated using P-N junctions formed by n-doping chemical vapor deposition grown graphene. Nano Letters. 2014;**14**:3702

[22] Xia F, Mueller T, Lin Y, Avouris P. Ultrafast graphene photodetector. Nature Nanotechnology. 2009;**4**:839

[23] Mueller T, Xia F, Avouris P. Graphene photodetectors for high-speed optical communications. Nature Photonics. 2010;**4**:297

[24] Liu C, Chang Y, Norris TB, Zhong Z. Graphene photodetectors with ultra-broadband and high responsivity at room temperature. Nature Nanotechnology. 2014;**9**:273

[25] Dou Y, Zhang L, Xu X, Sun Z, Liao T, Dou SX. Atomically thin non-layered nanomaterials for energy storage and conversion. Chemical Society Reviews. 2017;**46**:7338-7373

[26] Velicky M, Toth PS. 2D Materials in electrochemistry. Applied Materials Today. 2017;**8**:68

[27] Radisavljevic B, Radenovic A, Brivio J, Giacometti V, Kis A. Single-layer MoS2 transistors. Nature Nanotechnology. 2011;**6**:147

[28] Braga D, Gutiérrez Lezama I, Berger H, Morpurgo AF. Quantitative determination of the band gap of WS2 with ambipolar ionic liquid-gated transistors. Nano Letters. 2012;**12**:5218

[29] Chernikov A, Berkelbach TC, Hill HM, Rigosi A, Li Y, Aslan OB, et al. Exciton binding energy and nonhydrogenic rydberg series in monolayer WS2. Physical Review Letters. 2014;**113**:076802

[30] Mak KF, He K, Lee C, Lee GH, Hone J, Heinz TF, et al. Tightly bound trions in monolayer MoS2. Nature Materials. 2013;**12**:207

[31] Yin Z, HH Li HHL, Jiang L, Shi Y, Sun Y, et al. Single-Layer MoS2 phototransistors. ACS Nano. 2012;**6**:74

[32] Lopez-Sanchez O, Lembke D, Kayci M, Radenovic A, Kis A. Ultrasensitive photodetectors based on monolayer MoS2. Nature Nanotechnology. 2013;**8**:497

[33] Khan MF, Iqbal MW, Iqbal MZ, Shehzad MA, Seo Y, Eom J. Temperature dependent phonon shifts in single-layer WS2. ACS Applied Materials & Interfaces. 2014;**6**:21645

[34] Tsai DS, Liu KK, Lien DH, Tsai ML, Kang CF, Lin CA, Li LJ, He JH. Few-layer MoS2 with high broadband photogain and fast optical switching for use in harsh environments. ACS Nano. 2013;**7**:3905

[35] Lu J, Lu JH, Liu H, Liu B, Chan KX, Lin J, Chen W, Loh KP, Sow CH. Improved photoelectrical properties of MoS2 films after laser micromachining. ACS Nano. 2014;**8**:6334

[36] Zhang W, Chiu MH, Chen CH, Chen W, Li LJ, Wee ATS. Monolayer MoSe2 grown by chemical vapor deposition for fast photodetection. ACS Nano. 2014;**8**:8653

[37] Hwan Lee S, Lee D, Sik Hwang W, Hwang E, Jena D, Jong Yoo W. High-performance photocurrent generation from two-dimensional WS2 field-effect transistors. Applied Physics Letters. 2014;**104**:193113

[38] Perea-López N, Elías AL, Berkdemir A, Castro-Beltran A, Gutiérrez HR, Feng S, et al. Photosensor device based on few-layered WS2 films. Advanced Functional Materials. 2013;**23**:5511

[39] Huo N, Yang S, Wei Z, Li SS, Xia JB, Li J. Photoresponsive and gas sensing field-effect transistors based on multilayer WS2 nanoflakes. Scientific Reports. 2014;**4**:5209

[40] Yao JD, Zheng ZQ, Shao JM, Yang GW. Stable, highly-responsive and broadband photodetection based on large-area multilayered WS2 films grown by pulsed-laser deposition. Nanoscale. 2015;**7**:14974

[41] Chena Q, Marcoa ND, Yang Y, Song T, Chen C, Zhao H, et al. Under the spotlight: The organic–inorganic hybrid halide perovskite for optoelectronic applications. Nano Today. 2015;**10**:355

[42] Eperon GE, Stranks SD, Menelaou C, Johnston MB, Herz LM, Snaith HJ. Formamidinium lead trihalide: A broadly tunable perovskite for efficient planar heterojunction solar cells. Energy & Environmental Science. 2014;**7**:982

[43] Kojima A, Teshima K, Shirai Y, Miyasaka T. Organometal halide perovskites as visible-light sensitizers for photovoltaic cells. Journal of the American Chemical Society. 2009;**131**:6050

[44] Stranks SD, Eperon GE, Grancini G, Menelaou C, Alcocer MJP, Leijtens T, Herz LM, Petrozza A, Snaith HJ. Electron-hole diffusion lengths exceeding 1 micrometer in an organometal trihalide perovskite absorber. Science. 2013;**342**:341

[45] Xing G, Mathews N, Sun S, Lim SS, Lam YM, Grätzel M, Mhaisalkar S, Sum TC. Long-range balanced electron- and hole-transport lengths in organic-inorganic CH3NH3PbI3. Science. 2013;**342**:344

[46] DM Jang KP, DH Kim JP, Shojaei F, Kang HS, et al. Nano Letters. 2015;**15**:1591

[47] Liu J, Xue Y, Wang Z, Xu ZQ, Zheng C, Weber B, et al. Two-dimensional CH3NH3PbI3 perovskite: Synthesis and optoelectronic application. ACS Nano. 2016;**10**:3536

[48] Wang Y, Guan X, Li D, Cheng H, Duan X, Lin Z, Duan X. Chemical vapor deposition growth of single-crystalline cesium lead halide microplatelets and heterostructures for optoelectronic applications. Nano Research. 2017;**10**:1223

[49] Yu Y, Zhang D, Kisielowski C, Dou L, Kornienko N, Bekenstein Y, et al. Atomic resolution imaging of halide perovskites. Nano Letters. 2016;**16**:7530

[50] Dang Z, Shamsi J, Palazon F, Imran M, Akkerman QA, Park S, et al. In situ transmission electron microscopy study of electron beam-induced transformations in colloidal cesium lead halide perovskite nanocrystals. ACS Nano. 2017;**11**:2124

[51] Akkerman QA, Motti SG, Kandada ARS, Mosconi E, D'Innocenzo V, Bertoni G, et al. Solution synthesis approach to colloidal cesium lead halide perovskite nanoplatelets with monolayer-level thickness control. Journal of the American Chemical Society. 2016;**138**:1010

[52] Shamsi J, Dang Z, Bianchini P, Canale C, Di Stasio F, Brescia R, et al. Colloidal synthesis of quantum confined single crystal CsPbBr3 nanosheets with lateral size control up to the micrometer range. Journal of the American Chemical Society. 2016;**138**:7240

[53] Li J, Luo L, Huang H, Ma C, Ye Z, Zeng J, He H. 2D behaviors of excitons in cesium lead halide perovskite nanoplatelets. Journal of Physical Chemistry Letters. 2017;**8**:1161

[54] Yang Z, Wang MQ, Qiu HW, Yao X, XZ Lao SJX, Lin ZH, Sun LY, Shao JY. Engineering the exciton dissociation in quantum-confined 2D CsPbBr3 nanosheet films. Advanced Functional Materials. 2018;**28**:1705908

[55] Song J, Xu L, Li J, Xue J, Dong Y, Li X, Zeng H. Monolayer and few-layer all-inorganic perovskites as a new family of two-dimensional semiconductors for printable optoelectronic devices. Advanced Materials. 2016;**28**:4861

[56] Lv L, Xu Y, Fang H, Luo W, Xu F, Liu L, et al. Generalized colloidal synthesis of high-quality, two-dimensional cesium lead halide perovskite nanosheets and their applications in photodetectors. Nanoscale. 2016;**8**:13589

[57] Lee Y, Kwon J, Hwang E, Ra C-H, Yoo WJ, Ahn J-H, et al. High-performance perovskite–graphene hybrid photodetector. Advanced Materials. 2015;**27**:41

[58] Wang Y, Zhang Y, Lu Y, Xu W, Mu H, Chen C, et al. Hybrid graphene–perovskite phototransistors with ultrahigh responsivity and gain. Advanced Optical Materials. 2015;**3**:1389

[59] Qian L, Sun Y, Wu M, Xie D, Ding L, Shi G. A solution-processed high-performance phototransistor based on a perovskite composite with chemically modified graphenes. Advanced Materials. 2017;**29**:1606175

[60] Wang Y, Guan X, Li D, Cheng H, Duan X, Lin Z, Duan X. Chemical vapor deposition growth of single-crystalline cesium lead halide microplatelets and heterostructures for optoelectronic applications. Nano Research. 2017;**10**:1223

[61] Cheng HC, Wang G, Li D, He Q, Yin A, Liu Y, et al. van der waals heterojunction devices based on organohalide perovskites and two-dimensional materials. Nano Letters. 2016;**16**:367

[62] Ma C, Shi Y, Hu W, Chiu MH, Liu Z, Bera A, et al. Heterostructured WS2/CH3NH3PbI3 photoconductors with suppressed dark current and enhanced photodetectivity. Advanced Materials. 2016;**28**:3683

[63] Kang DH, Pae SR, Shim J, Yoo G, Jeon J, Leem JW, et al. An ultrahigh-performance photodetector based on a perovskite–transition-metal-dichalcogenide hybrid structure. Advanced Materials. 2016;**28**:7799

[64] Lu J, Carvalho A, Liu H, Lim SX, Castro Neto AH, Sow CH. Hybrid bilayer WSe2–CH3NH3PbI3 organolead halide perovskite as a high-performance photodetector. Angewandte Chemie, International Edition. 2016;**55**:11945